scientific reports

Check for updates

OPEN

Going beyond hardware limitations with advanced stray light calibration for the Metop-3MI space instrument

L. Clermont✉, C.Michel, Q. Chouffart & Y. Zhao

Space optical instruments play a pivotal role in enhancing our understanding of the universe and our planet, and are crucial in addressing the urgent challenges posed by climate change. In this context, stray light has emerged as a primary performance limitation. Originating from ghost reflections or scattering, it obscures essential details and introduces false information into images. With the demand for increasingly high-performing instruments, mitigation through hardware optimization is becoming insufficient. We are entering an era where future instruments require a stray light correction algorithm to meet user specifications, necessitating extensive on-ground calibration. This paper examines the Metop-3MI Earth observation instrument, which, with wide field of view, broad spectral range, and multi-polarization capabilities, epitomizes the challenges of stray light calibration and correction. A custom calibration apparatus was constructed to evaluate the complex stray light dependence on field-of-view, wavelength, and polarization. Data were processed, and stray light kernels database was derived, which then fed into a specially developed correction algorithm. Applied to the image of an extended scene, it effectively reduces stray light by a remarkable factor of 91. This achievement sets a new standard for low-stray-light instruments and provides a comprehensive case study for future missions.

Space optical instruments are remarkable tools for unlocking the secrets of the universe and deepening our understanding of the Earth. Over the years, innovations in design, manufacturing, and detector technologies have significantly enhanced their capabilities[1–4]. However, in the most demanding applications, stray light (SL) has emerged as a primary performance limitation. Originating from ghost reflections or scattering, SL degrades image quality by introducing artifacts[5,6]. It obscures essential details and introduces false information, thereby limiting the valuable insights that can be gained from satellite imaging.

Earth observation is an application where SL is particularly critical[7]. In that case, instruments require strict radiometric accuracy, which can be compromised by SL coming from a broad range of angles, as the Earth acts as an extended source[8]. SL is also critical in any instrument observing high-contrast scenes or faint objects[9]. For example, coronagraphs need to maintain low SL from bright stars to detect nearby faint objects like exoplanets[10–13]. Similarly, in heliospheric imagers, minimizing SL from the sun is crucial for observing the solar wind[14–17]. The primary method for reducing SL involves optimizing the opto-mechanical design[18–22], including the use of baffling, black treatment[23,24] and anti-reflection coatings[5,6]. However, as we reach the limits of what can be achieved through hardware alone, SL correction algorithms are becoming necessary[25,26]. In this regard, Metop-3MI is among the most pivotal missions.

Metop-3MI aims to study the chemical composition of the atmosphere, analyze clouds and aerosol properties and measure the Earth's albedo[27–29]. These tasks are essential for understanding climate evolution and monitoring air quality, areas of increasing concern amidst climate change. Metop-3MI is equipped with two wide-field imagers (± 57°) operating in the Visible and Near infrared (VNIR: 410–910 nm) and short-wavelength infrared (SWIR: 910–2130 nm). It features multi-spectral and multi-polarization capabilities, utilizing an on-axis refractive configuration and a rotating filter wheel. Orbiting in low-Earth orbit, it will conduct observations across various wavelengths and polarizations, with a total of 21 channels in VNIR and 9 in SWIR. A few channels are non-polarized (*NP*). For all the others, there are three channels per wavelength, each with a different polarization orientation (*P*): 0° and 60° and − 60°.

Centre Spatial de Liège, STAR Institute, Université de Liège, Avenue du Pré-Aily, 4031 Liège, Belgium. ✉email: lionel.clermont@uliege.be

Despite an optimized design, significant SL is caused by hundreds of ghost reflections[25,26,30,31]. Additionally, roughness and contamination on optical surfaces cause further SL through scattering[30–32]. Therefore, in observations of high contrast extended scenes, light from bright areas generates SL, adversely impacting darker regions[25]. Crucial details are obscured, and, for example, the SL signal could mistakenly be interpreted as originating from aerosols in the atmosphere[33]. According to user requirements, for a reference extended scene with a field of view half-illuminated by a bright radiance (L_{max}) and half by a dark radiance ($L_{ref} \approx 0.1 \cdot L_{max}$), SL across the dark region—excluding the area within 5 pixels from the transition—must not exceed 0.17% of L_{ref}. However, ray tracing simulations predict a SL level two orders of magnitude above that, underscoring the need for a SL correction algorithm. We previously developed an algorithm concept[25], predicting using simulations a SL reduction factor of 119. Its fundamental principle involves estimating the SL for any given input scene and subtracting it from the measurement. This is achieved using a linear combination of SL kernels across the field of view, where each kernel is modulated by the measured signal at that specific field.

Building a correction algorithm for Metop-3MI requires to perform an extensive on-ground calibration of the SL properties. The calibration is among the most challenging ever conducted, evaluating SL properties across thousands of illumination conditions. Furthermore, measurements are performed under thermal-vacuum conditions to accurately simulate the space environment[34]. This mission is among the first to prioritize such an extensive and complex calibration campaign in advance, a strategy informed by lessons learned from the POLDER mission[35] in the early 2000s, which had a similar but simpler design configuration. In POLDER, SL was initially not anticipated to be a critical issue. On-ground testing was performed only at a late stage, shortly before launch, where SL issues were unexpectedly discovered. This yielded valuable insights, particularly the complex dependence of SL with respect to the field of view, wavelength, and polarization[35]. Metop-3MI has even more demanding SL performance requirements, in fact POLDER didn't had a specific target. In other situations, SL properties is simpler. For example, in the three-mirror anastigmat instrument ProbaV, SL primarily arises from mirror scattering[22]. This results in a straightforward SL profile that diminishes continuously away from the nominal signal, necessitating only a few calibration measurements to develop a deconvolution algorithm[36–38].

Metop-3MI marks a paradigm shift in SL calibration and correction practices, pushing further than even the complexity of testing methods and subsequent processing. With the demand for ever-greater precision in space telescopes, future instruments are expected to systematically undergo such extensive and precise SL calibration, together with the use of an advanced SL correction algorithm. This necessity is further highlighted by instances where SL was only discovered in space, such as with TIRS on board Landsat[39–41], GAIA[42] and very recently EUCLID[43]. For example, FLEX[44] and ALTIUS[45] are Earth observation missions, currently in development, where a priority is put on SL calibration. In this paper, we delve into the intricacies of the Metop-3MI SL calibration, focusing specifically on the Proto-Flight model—the first of three models planned for space launch. We detail the SL measurement and data processing techniques, focusing on the SL coming from sources located inside the instrument field-of-view. Calibration data are then introduced into a correction algorithm, which is subsequently tested with on-ground extended scene measurements to effectively demonstrate SL removal. We evaluate the correction performance and demonstrate an SL reduction factor of up to 91. Finally, we extract valuable lessons for future missions.

Methods and results

SPST measurements

The SL calibration involves measuring the Spatial Point Source Transmittance (SPST), corresponding to the SL pattern observed on the detector when the instrument is illuminated by a point-like source at infinity[25] (equivalent to a collimated beam). The instrument is vertically positioned to minimize gravity-induced deformation and ensure optimal functioning of the heat pipes. Above the instrument, an illumination device produces a collimated beam using an off-axis parabola with fiber injection (Fig. 1a). It is fed with a white light source for the VNIR and a laser for the SWIR. The beam nominally illuminates one pixel, while the signal on the other pixels originates from SL (Fig. 1b). Signals on the detector are expressed in units of digital number; the SPST is unitless as it is the SL signal normalized to the nominal signal. The nominal signal represents the instrument's nominal performance, including the effects of lens transmission.

A mechanical device adjusts the illumination angle for SPST measurements across a pre-defined calibration grid, which was optimized using ray tracing data[25]. Figure 1c depicts the grid in the angular domain, where θ and ϕ represent the elevation and azimuth angles. Figure 1d shows the corresponding nominally illuminated pixels on the detector, denoted as (x_f, y_f). In addition, the mechanical device enables a scan of the collimator over the instrument's aperture, compensating for its limited size. Indeed, while the collimator is sufficiently large to cover the entrance pupil of the instrument, effectively acquiring the nominal signal, SL can originate from rays illuminating the instrument outside of that pupil. Hence, for each field angle, the total SL is obtained by summing the acquisition for the different scan positions. Instead of scanning the entire aperture, requiring up to 25 positions, we perform a selective scan over the SL Entrance Pupil (SLEP)[30,31]. This pupil represents the area where incoming rays contribute to SL reaching the detector (Fig. 1e). Outside of the SLEP, SL rays are blocked before reaching the detector. Computed by ray tracing with ghosts up to the second level, the SLEP is covered with only 2 to 4 scan positions, except for $\theta < 3°$, where up to 15 positions are needed. With a positioning accuracy of approximately 10 microns, overlaps or gaps between scans are negligible. Additionally, the laser power remains stable during acquisitions at various scan positions.

SL is measured over a high dynamic range by combining measurements at different integration times (VNIR: 20ms to 20s, SWIR: 0.1 ms to 100 ms) and various input beam powers. Input power is varied using a 4F setup[46,47] with adjustable slits before the collimator's fiber injection. As shown on Fig. 1f, the 4F setup employs an off-axis

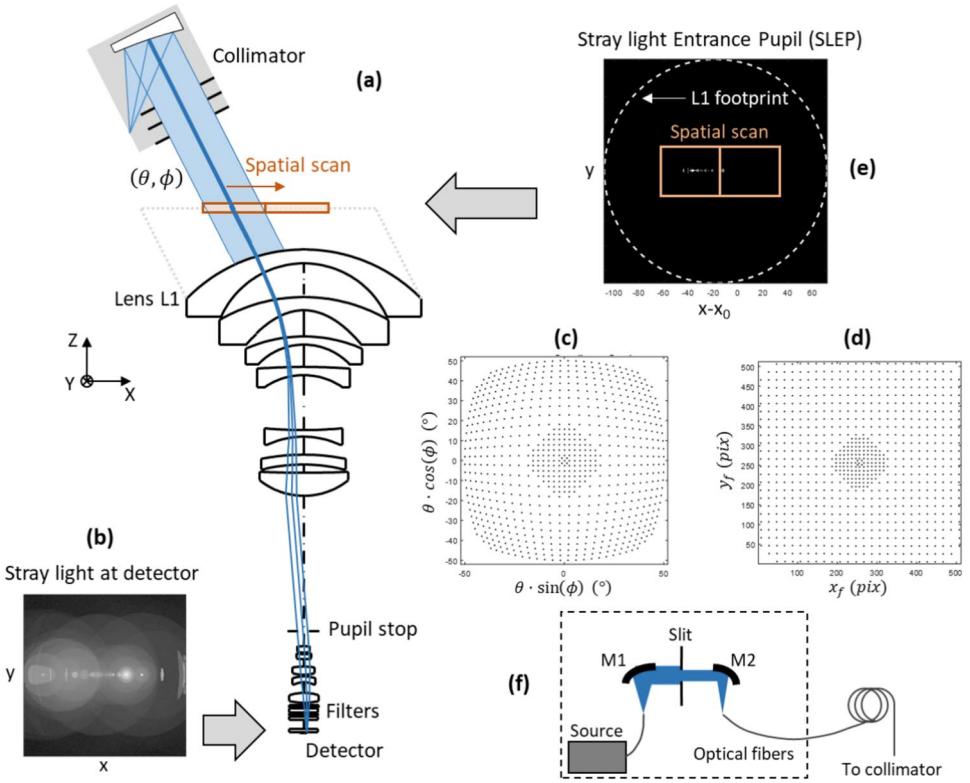

Figure 1. (**a**) Sketch of the experimental setup for characterizing SPST maps. (**b**) Stray light at the detector. (**c**) Calibration grid in the angular domain. (**d**) Calibration grid at detector level. (**e**) Stray light Entrance Pupil. (**f**) Source attenuation mechanism.

parabola to collimate the beam of light, while a second off-axis parabola focuses the light into the fiber. Two pairs of slits can be gradually closed to decrease the amount of light injected into the fiber.

SPST reconstruction

The dynamic range decomposition employs three levels, as depicted in the example of Fig. 2a. Level L1, characterized by the shortest integration time and lowest beam power, captures the nominal signal, while leaving the SL within the noise. Level L2, utilizing a higher beam power, saturates the nominal signal but succeeds in capturing the SL directly surrounding it. Finally, Level L3 combines high beam power with an increased integration time to capture the remaining SL. This enables the characterization of SL features down to a dynamic range of 10^{-8}, which is far better than the capabilities of the detector with a single acquisition.

For each level, measurements from different spatial scans are summed. Each acquisition undergoes dark current correction by subtracting a reference dark map, previously acquired with the same integration time. In VNIR, measurements are corrected for smearing, estimating its amplitude on each line using a smearing accumulation column at the detector's edge. High beam power generates a non-uniform smearing profile, previously characterized and removed from each acquisition. The SWIR detector, unaffected by smearing, employs an anti-blooming apparatus. However, in SWIR, pixels directly adjacent to saturated ones are impacted by artifacts and are therefore excluded from measurements, across about 5 pixels.

Maps at L1, L2, and L3 are recombined using a stitching approach, calculating the median of the ratio between pixels around the saturated area. This is necessary to compensate for the use of different input power and integration times across levels. The process begins with the L3 map, retaining only signals from unsaturated pixels. Subsequently, a scale factor is applied to the L2 map to align its signal level with that of L3. This factor is derived from the ratio of signals, for the L2 and L3 maps, in the pixels surrounding L3's saturated area. The signal for the missing pixels of the L3 map is then taken from the L2 map. The same process is applied to the L1 map to address signals from pixels saturated at L2. Finaly, recombined maps are normalized to the nominal signal. However, due to the collimator's orientation (elevation and azimuth angles) not being precisely centered on a pixel, the nominal signal may span up to a 2×2 pixel area. Thus, the nominal is defined as the sum of the signal across these four pixels. After normalization, the SPST is obtained by setting the signal in these pixels to zero, thereby keeping only the SL on the map.

Figure 2b presents SPST maps measured at various field angles (410 nm, $P = -60°$). In comparison, Fig. 2c shows the maps predicted by ray tracing, and Fig. 2d depicts the radial profiles passing through the center of the detector and the nominal position. The maps reveal a complex superposition of hundreds of ghosts, varying in shape and amplitude and aligned along the radial direction. SL is especially pronounced around the nominal

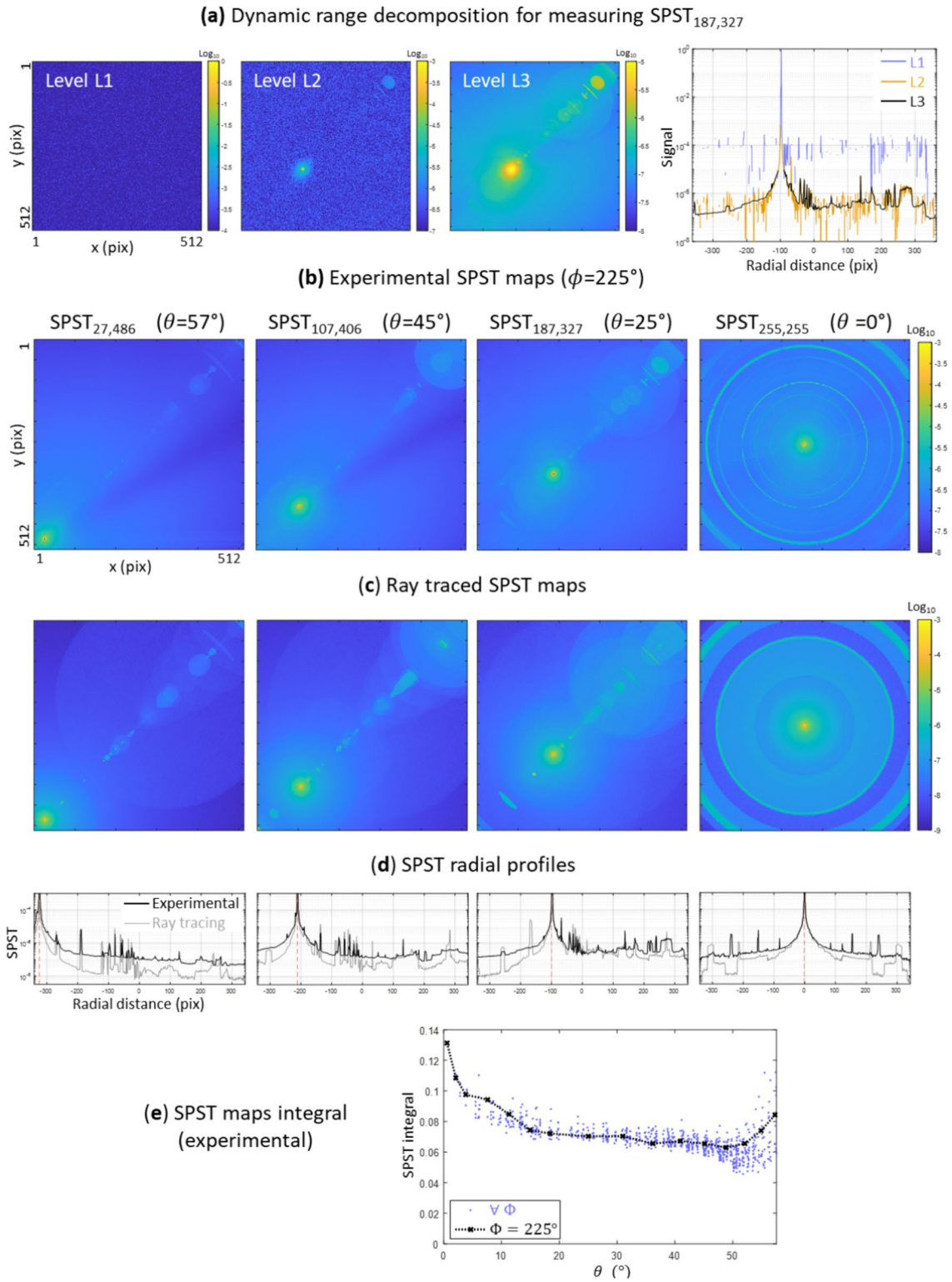

Figure 2. (**a**) Acquisitions of the SL is done with three levels of dynamic range decomposition. Measured (**b**) and ray traced (**c**) SPST maps for various fields (410 nm, P = -60°), and associated radial profiles (**d**). (**e**) Evolution of the SPST maps integral as a function of θ, for all values of ϕ.

pixel, due to ghost reflections occurring near the detector and scattering at lens interfaces. Experimental results align with ray tracing predictions in terms of geometry but not in ghost's amplitude. Additionally, two unexpected effects are observed. First, for some fields we observe a thin line at a 14° angle from the vertical axis, centered on

the nominal pixel and likely due to a lens scratch or contamination. This is visible on Fig. 2b at $\theta = 0°$. Second, we observe a shade in the SL's diffuse part, present only in polarized channels at smaller wavelengths, due to a polarization effect on the light scattering. The shade is systematically aligned with the channel's polarization orientation.

Figure 2e depicts the evolution of the integral of the measured SPSTs with θ for all values of ϕ on the calibration grid. A dispersion of the data points is observed, due not to noise in the acquisitions, but rather to an asymmetry of the instrument along ϕ. For a specific value of ϕ, here 225°, the evolution is smooth.

SLEP validation

Measuring SL with a SLEP-limited scan reduces the duration of measurements compared to a full scan across the instrument's aperture. To verify the SLEP's efficiency in capturing all SL features, several verification measurements are conducted using a full spatial scan. Figure 3a, b illustrate an SPST map measured with the SLEP method and with a full scan, respectively, at the 910nm non-polarized channel. Their radial profiles are presented in Fig. 3d. This comparison confirms that all ghosts detected with the full scan are also captured by the SLEP, underscoring its effectiveness. Note that in this channel, a very slight residual horizontal smearing line is visible.

Another observation is that the full scan measurement reveals a more pronounced background scattering signal. Although this effect is less pronounced at shorter wavelengths, at 910 nm, SLEP measurements show scattering vignetted outside a rectangular area near the nominal. This occurs as some scattering happens when rays illuminate the instrument outside the SLEP. This smooth scattering pattern can be represented using a simple Harvey model[5]. Therefore, for each SPST measured with the SLEP, this scattering component is numerically incorporated. Figure 3c illustrates the SPST resulting from adding this model to the SLEP measurement, effectively replicating the SL achieved with the full spatial scan.

SPST polarization dependence

L1 and L2 maps are calibrated for each channel while the filter wheel rotates continuously. L3 maps are characterized with stationary filter wheel, allowing for extended integration times. To shorten the campaign duration, only non-polarized channels and those with a polarization orientation $P = -60°$ undergo full calibration at L3. Nevertheless, the polarization dependence is evaluated by taking extra measurements for $P = 0°$, 60° and − 60°, at a few elevation angles and in 30° steps for the azimuth.

Figure 4a displays L3 maps for $P = -60°$ (410nm), at $\theta = 14°$ across various azimuth angles ϕ. The maps reveal a shade in the SL's diffuse part, aligned with the polarization axis regardless of ϕ. A ghost is observed, its amplitude varying with ϕ, peaking when the azimuth aligns with the polarization orientation ($\phi = 60°$), and reaching a minimum in the perpendicular direction ($\phi = 150°$). Decomposing the map by spatial scans, as shown in Fig. 4b, reveals that this specific ghost is present only in the third scan position, while the shade is in scan one. When the signal of the ghost is integrated, Fig. 4c emphasizes a variation with ϕ following Malus's law[48], valid for the channels at any polarization orientations. This behavior persists for θ between 11° and 17°. Outside this range, the ghost is vignetted before reaching the detector.

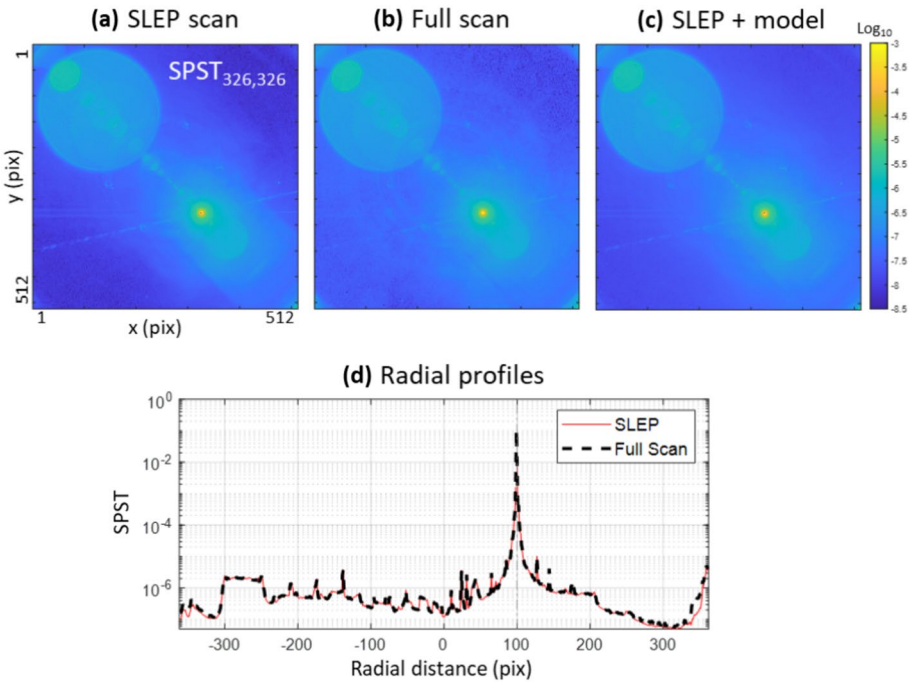

Figure 3. SPST (910 nm) measured with a scan restricted to the SLEP (**a**) or a full scan (**b**). (**c**) Map with SLEP-limited scan with scattering model added to replicated the full scan measurement. (**d**) Radial profiles for SLEP and full scan measurements.

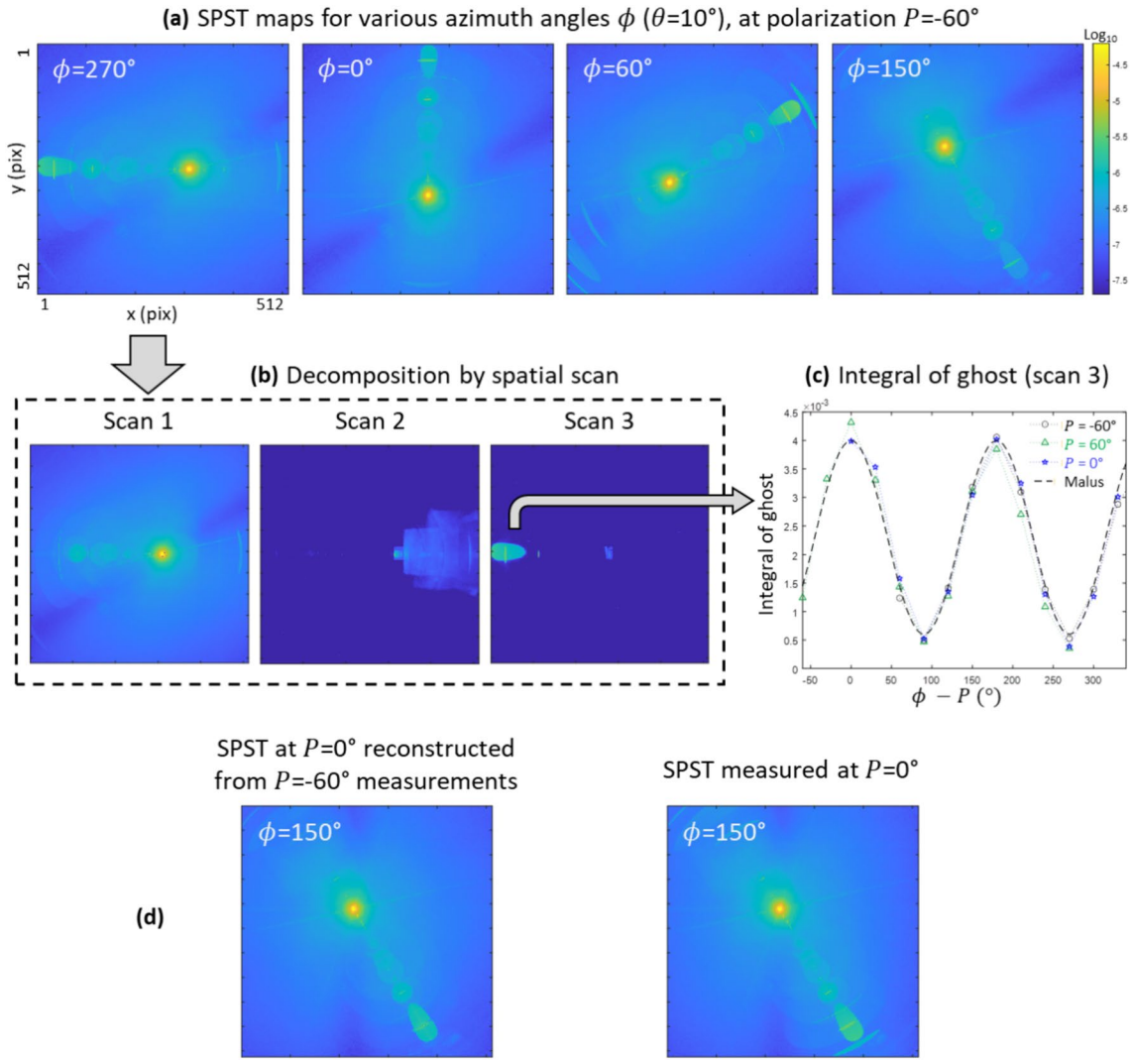

Figure 4. (**a**). SPST maps for various azimuth angles ϕ (410 nm, P = -60°, θ = 10°). (**b**) Decomposition by spatial scan of the SPST at ϕ = 270°. (**c**) Evolution of the integral of scan 3's ghost, as a function of ϕ, for channels at different polarizations P. (**d**) SPST at P = 0°, measured directly or reconstructed from measurements at P = -60°.

SPST maps at polarizations 60° and 0° are constructed by recombining L3 maps calibrated at − 60°. Subsequent transformations are applied to accurately replicate polarization effects. The ghost previously discussed is modulated to align with Malus's law for the channel's polarization orientation. Additionally, the shade is modeled, removed from the image, and then reintroduced at the desired orientation. Figure 4d showcases an example of an SPST map reconstructed at P = 0°, effectively replicating the verification map measured at the same polarization. Ultimately, the relative residual polarization error on a single SPST map for P = 0° and 60° is between 1.1% and 3.6% for the VNIR channels (details in appendix 4.9). When considering an extended scene, the error will be smaller because the positive and negative errors in SPST associated with different field angles will partially compensate for each other. This error comes mainly from residual polarization effects on scan position number one, with many ghosts superposed that can't be individually adapted for polarization. In SWIR, polarization effects are negligible.

SPST field-of-view interpolation

Interpolation is performed to create an SPST database over a field-of-view grid denser than the calibration grid, serving as input kernels for the SL correction algorithm. The interpolation process, based on a local symmetry assumption, applies rotation and scaling transformations to SPST from nearest calibrated fields[25]. The rotation adjusts the azimuth angle, while the scaling adjusts the elevation angle associated to the map. This effectively relocates various SL patterns to their approximate intended positions. To prevent unwanted rotations of the scattering tilted line and polarization shade, these elements are removed before any transformation is applied. Afterward, the line is reinstated at its original orientation, and the shade is positioned according to the channel's polarization orientation. This is achieved by modeling the shade and line patterns, then performing a simple subtraction from the original map followed by an addition to the interpolated map.

Figure 5a depicts an example of an interpolated SPST map, closely matching the verification map measured at the same field Fig. 5b. Radial profiles are shown in Fig. 5c. While excellent correspondence is found, interpolation introduces some errors in positioning and size of SL features. This can be visualized by computing the ratio of the interpolated map to the verification map, as illustrated in Fig. 5d. A ghost on the interpolated map that is precisely positioned as on the verification map gives a ratio of 1. Any slight displacement results in a ratio below 1 on one side of the ghost and above 1 on the other side. Such displacement error is evident when zooming in on localized ghosts in Fig. 5d. Here, the error extends over approximately 3 pixels, similarly to the one depicted in Fig. 5e, obtained with ray-traced maps in the same conditions. With ray-traced maps, it was previously demonstrated[25] that interpolation errors limit the correction factor to × 119 on the reference extended scene used for validating users requirements. As the interpolation error on measured maps is similar to that in ray-traced maps, the impact on the correction algorithm performance is comparable as well.

Once the maps are interpolated, the near-nominal area is smoothed by averaging the signal within a 5-pixel radius from nominal position. This compensates for the fact that illumination is not perfectly centered on the nominal pixel, affecting SL distribution around that area. The choice of a 5-pixel radius is directly linked to user specifications, which assess SL correction at 5 pixels from a transition.

Reference extended scene estimated SL

Figure 6a presents the theoretical signal for the reference extended scene used for validating users requirements. Half of the field-of-view is illuminated with bright radiance while the other half has a dark radiance. Out-of-field is not illuminated. Figure 6b depicts the corresponding SL pattern, estimated using the interpolated SPST database. The estimation involves summing SPSTs across the field of view, each modulated by the nominal signal at their corresponding field angles. Figure 6c displays horizontal profiles of the nominal and SL patterns. The initial SL level for the reference extended scene is obtained by calculating the statistical value at the 1 sigma percentile across the darker area, excluding within 5 pixels of the transition. In VNIR, this results in SL level between 11.4% and 21.7% of L_{ref} in the darker area, depending on the wavelength. In SWIR, SL ranges between 22.4 and 27.6% of L_{ref}.

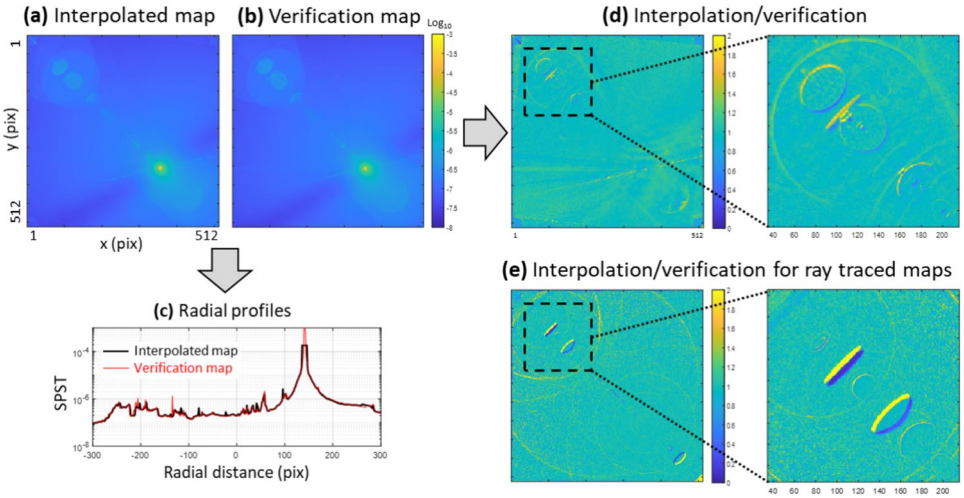

Figure 5. Interpolated map at an intermediary field (**a**) and verification map measured at the same field (**b**). (**c**) Radial profiles of the maps. Ratio of the interpolated and verification maps for the experimental measurements (**d**) and the case of ray traced maps (**e**).

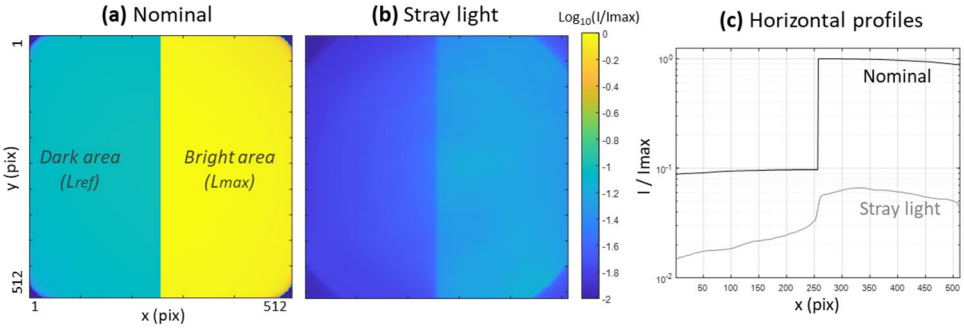

Figure 6. Reference extended scene (410 nm) nominal signal (**a**) and corresponding SL (**b**). (**c**) Horizontal profiles.

Extended scene measurement

A measurement of the reference extended scene is not feasible in a laboratory setting, as it would require a giant integrating sphere at a large distance from the instrument. Instead, a scaled-down version is obtained by positioning a smaller integrating sphere with square aperture in front of the instrument (Fig. 7a). By rotating the sphere, the instrument captures a finite sized scene from various positions within its field of view. Figure 7b.1 displays a measurement outcome, with a bright square representing the nominal image of the scene, surrounded by SL features. Given the limited dynamic range of a scene (SL/nominal), a single level measurement suffices. By combining measurements from the sphere at various positions, an extended scene covering half the field of view while the other half is dark is reproduced (Fig. 7c.1). A perfectly uniform scene is not possible due to inevitable overlaps in sphere positioning.

The limitation of this setup is the imperfect coverage of the SLEP by the sphere's aperture. This leads to some missing SL because the SLEP of the nominally illuminated field angles is not fully covered. Conversely, it results in additional SL as the sphere overlaps the SLEP of field angles that are not nominally illuminated. Additionally, the sphere illuminates the instrument's environment, resulting in some signal originating from the instrument observing its surroundings, even if black-coated.

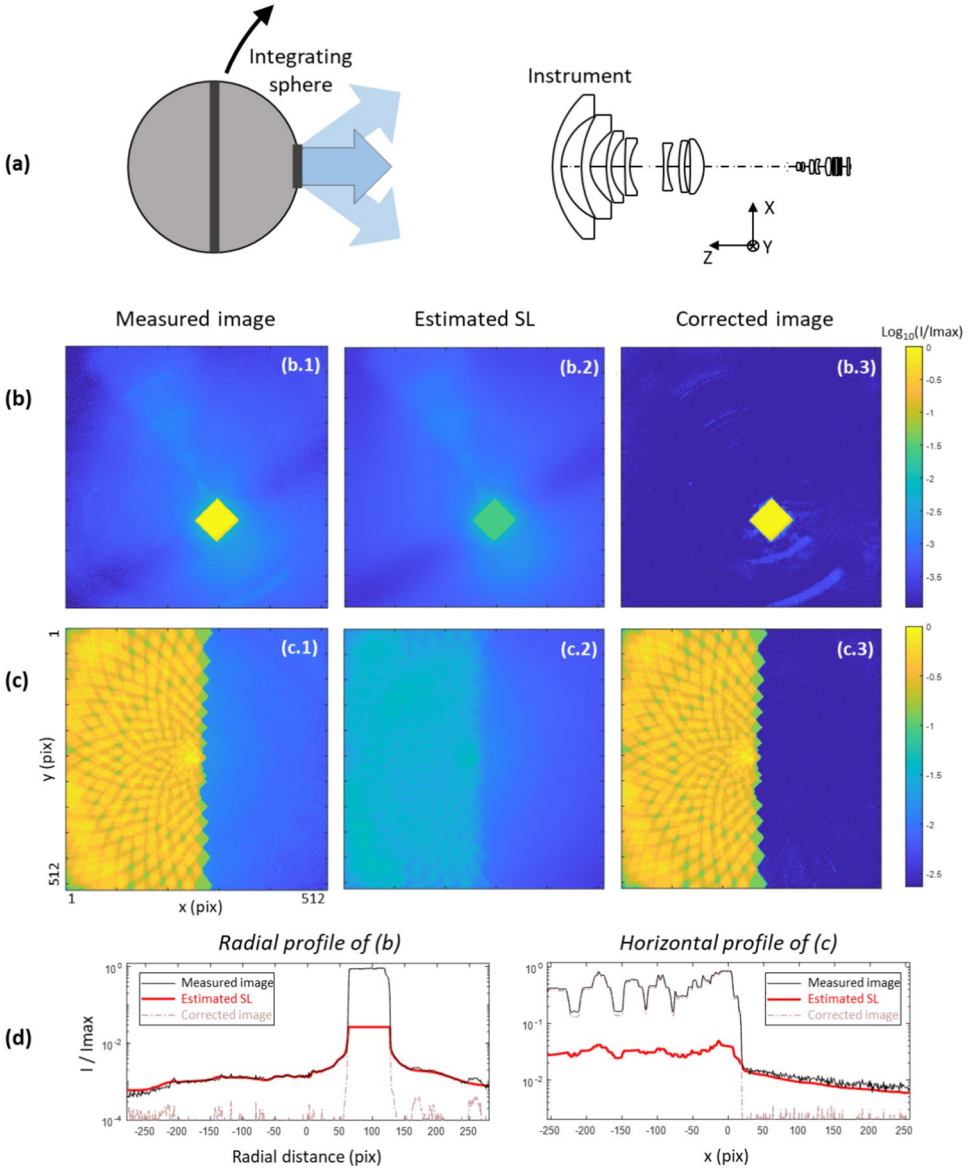

Figure 7. (**a**) Experimental setup for the extended scene measurement. (**b.1**) shows the measured image when the instrument is illuminated by an integrating sphere at a single position, (**b.2**) shows the estimated SL pattern associated to that measurement, calculated with the correction algorithm. (**b.3**) shows the corrected image with the correction algorithm. (**c**) Shows similar results as (**b**) but with a large extended scene obtained by combining measurements of the integrating sphere at different positions. (**d**) Profiles of the maps.

Extended scene correction

SL correction involves estimating the SL pattern associated with a given input scene. A first estimation is obtained by summing SPSTs across the field of view, each modulated by the measured signal at their corresponding field angles. However, a residual error remains, because the SPSTs are modulated by a map including SL. Subtracting this initial result from the measured signal provides a first estimate of the corrected map. More refined estimation is achieved through a second iteration, modulating SPST maps by the first estimation of the corrected map.

Figure 7b.2 displays the estimated SL for the extended scene measurement taken with the sphere in a single position. Remarkably, the estimation closely matches the actual measurement, capturing details such as ghosts and polarization shade. The shape of the nominal square is still visible, because of bright SL present directly in the nominal region. Figure 7b.3 presents the corrected map, where most of the SL has been eliminated. However, some residual SL persists, a consequence of the measurement's limitations due to imperfect SLEP coverage and environment illumination. Figure 7c.2,c.3 show similar results for the large extended scene with only half the field-of-view illuminated. Here also, SL is similar to that of the measurement and the corrected image has most of it eliminated. Profiles of the maps are show on Fig. 7d.

SL correction performance

The correction of the experimental extended scene offers a valuable qualitative demonstration. However, due to the setup's limitations, it is not suitable for quantitative performance assessments. Instead, compliance with user specifications for the reference extended scene is assessed through error budget modeling (details in appendix 4.9). This approach identifies and individually assesses various factors contributing to residual SL error. Key contributors include detector noise, dark correction, and stitching imprecision during the recombination of different levels. Furthermore, for channels with $P = 60°$ and 0°, an additional source of error is the imperfect transformation of L3 maps from measured at $P = -60°$. Total residual SL error is determined by statistically combining these individual contributors, considering 1 sigma percentile.

Figure 8a presents the error budget for the 410 nm channels, showing the estimated initial SL level and residual SL after correction. Figure 8b displays the initial and residual SL across all channels. The correction factor, depicted in Fig. 8c, is the ratio of the residual and initial SL levels. In VNIR, non-polarized channels and those at $P = -60°$ achieve correction factors between 63 and 91. The exception is the 763 nm channel, with a correction factor of 26, as it uses kernels calibrated for the 765 nm channel, despite some differences. The difference between these channels arises from the slight variations in the reflectivity of their spectral filters. For channels at $P = 60°$ or 0°, the correction factor ranges from 26 to 61, with minimal impact from polarization.

Discussion and conclusions

In this study, we conducted an extensive SL calibration of Metop-3MI and built a correction algorithm for removing SL from in-flight measurements, pushing the performance beyond the hardware capabilities. This is particularly challenging due to a wide field-of-view, broad spectral range and multi-polarization channels, causing the presence of hundreds of ghosts with complex properties. SPST maps for various channels are acquired across

(a)

Wavelength (nm) Polarization	410 -60°	410 0° & 60°
Initial SL (% of Lref)	**21,72%**	**21,72%**
Residual SL after correction: individual contributors (% of Lref)		
Dark correction for L3	0,01%	0,01%
Dark correction for L2 & L1	0,015%	0,015%
Beam residual polarization	0,0022%	0,0022%
Level recombination error	0,13%	0,13%
Near-nominal smoothing	0,092%	0,092%
Normalization error	0,0024%	0,0024%
SNR on SPST maps	0,0035%	0,0035%
SPST maps interpolation processs	0,17%	0,17%
Algorithm binning and convergence	0,028%	0,028%
Polarization	-	0,79%
Residual SL after correction: total (% of Lref)	**0,25%**	**0,81%**
Correction factor	**85**	**27**

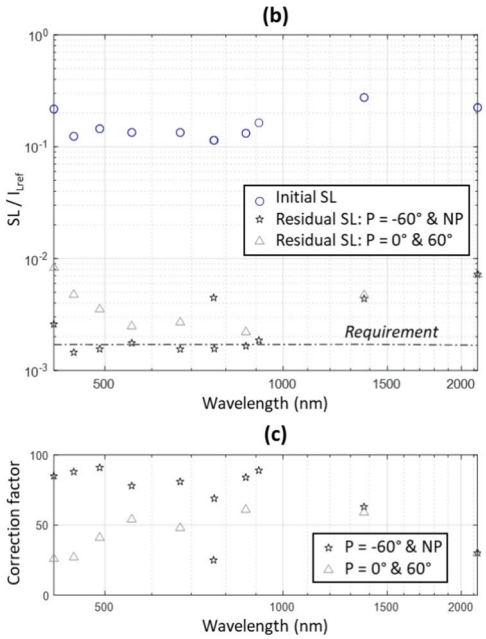

Figure 8. (**a**) Residual SL in the reference extended scene's dark area, evaluated at 1 sigma percentile, for 410 nm channels. Details are given in appendix 4.9. (**b**) Initial and residual SL for all channels. (**c**) SL correction factor.

hundreds of fields, accurately measuring features down to 10^{-8} with three level of dynamic range decomposition. A database of SPST maps over a dense field-of-view grid is obtained by interpolation, serving as an input for the SL correction algorithm. When applied to the image of an extended source, the algorithm successfully removes the SL while preserving the nominal image, with a remarkable correction factor up to 91.

The necessity for an instrument to remain vertical is challenging, as constructing an illumination device capable of fully illuminating its large aperture in a single acquisition is impractical. The solution implemented here uses a smaller device that is spatially scanned over the aperture. The SLEP approach effectively captures all ghost features while avoiding the need for a full spatial scan, which would have significantly prolonged the thermal vacuum testing campaign and led to unreasonable increases in cost. This requires for the SLEP to be determined in advance using ray tracing simulations, which was done here considering only ghosts up to the second order. In practice, SPSTs also include contributions from scattering at the lenses' interfaces. Most of this scattering is captured in the measurements since it occurs predominantly in the specular direction, involving rays that enter through the nominal entrance pupil which is included in the SLEP. Nevertheless, a smaller scattering contribution arises from rays hitting the instrument outside the defined SLEP, resulting in a smooth background signal on the detector. This effect was effectively replicated using a simple Harvey model.

SPSTs exhibit significant dependence on polarization orientation. However, measurements for all polarizations are conducted only at levels L1 and L2. Level L3, characterized by the longest integration times, contributes most significantly to the calibration duration. Therefore, measuring at L3 for a single polarization orientation effectively minimizes this duration. This approach necessitates transforming L3 maps from one polarization to another to construct SPSTs for all channels. For example, we found a polarized shade, and a large ghost evolving as per the Malus law with the azimuth angle. The SLEP scan decomposition facilitates its adaptation to another polarization as this ghost is isolated on scan three. Nevertheless, scan number one overlaps the nominal entrance pupil and generates hundreds of superposed ghosts. Their polarization dependance cannot be adapted, thus they contribute to a significant residual error. For future instruments, especially the next models of Metop-3MI to be sent into space after, the test campaign should encompass additional measurements at L3 of the scan one across all polarizations. This approach would lead to a reasonable increase in the campaign's duration, while completely eliminating the polarization error at scan one. Combined with the ghost modulation at scan three, this is expected to yield a consistent SL correction factor across all polarization orientations. In the SWIR, where cooled detectors are used, controlling contamination is crucial because it can alter the optical properties of the detector's surface and, consequently, the SL properties.

Defining, interpreting, and experimentally verifying SL requirements presents significant challenges. The Metop-3MI's reference extended scene, typical for Earth observation instruments, effectively replicates transitions between lands, oceans, and clouds. Although useful for ray tracing performance prediction during the design phase, it becomes impractical experimentally. In practice, SL requirements should be defined outside nominally illuminated areas. Indeed, within illuminated areas, it is impossible to distinguish SL from the nominal signal. Conversely, in completely dark areas, any signal exceeding the noise level is necessarily SL. Therefore, a reference extended scene where the entire field of view is illuminated, as in Metop-3MI, should be avoided, even if one side exhibits lower radiance than the other. Instead, the reference scene should include a completely dark area, and performance should only be assessed in this area.

Another aspect to consider is how the reference extended scene test can be implemented in a laboratory setting. To create a large, uniform extended scene, it requires placing a giant extended source far from the instrument. Alternatively, we achieved a scaled-down extended scene using a reasonably sized integrating sphere close from the instrument. However, this method is suitable only for qualitative performance assessments due to errors from imperfect SLEP coverage. Additionally, the integrating sphere illuminates the laboratory environment, which the instrument subsequently detects, introducing further inaccuracies. For Metop-3MI, quantitative assessment was derived from error budget modeling, which helps pinpoint the main error contributors, notably the polarization effect, followed by the interpolation process. An optimal scaled-down extended scene measurement could be performed by illuminating the instrument with a collimator whose field-of-view covers several pixels. For example, using a $10° \times 10°$ collimator would yield results similar to those from a scaled-down integrating sphere measurement but without its limitations. Optimal SLEP coverage can be achieved by spatially scanning the collimator above the instrument, while its restricted field-of-view prevents the illumination of the laboratory environment. Additionally, this measurement could be conducted from several angles, effectively verifying the SL requirements across different areas of the instrument's field-of-view. Combining several of these measurements, similarly as in Fig. 7c, would provide a broader extended scene. However, we must always preserve a non-illuminated area where the SL level can be assessed.

In addition to SL originating from sources within the field-of-view, instruments can also present out-of-field (OOF) SL. Ray tracing has shown previously[26] that OOF SL in Metop-3MI is, on average, 20 times smaller than in-field SL. Here, OOF SL can occur up to an elevation angle of 63°. The OOF SL level could be even lower with a longer fore-baffle[5], but this is not always possible due to volume constraints. Measuring and correcting OOF SL is significantly more complex than dealing with in-field SL because of the faint levels of SL and the absence of nominal signals on the detector. Therefore, the SPST can't be defined as the SL on the detector normalized to a nominal signal as with the in-field SL. Instead, the SL kernels must be normalized to the input irradiance, necessitating excellent collimator monitoring and gain characterization. We recently proposed a theoretical concept for an OOF SL correction algorithm[26], in which the SL kernels are modulated by the scene radiance. Although there is no nominal signal on the detector from OOF illumination, the OOF scene radiance in the along-track direction of the satellite can be deduced from successive images of the Earth. For the across-track direction, mirroring can be used to estimate the OOF radiance, although this method cannot predict localized objects such as clouds. Due to the complexity of OOF SL compared to in-field SL, the experimental results related to it will be presented in a future paper.

SL calibration is essential for developing SL correction algorithms, enabling space instruments to operate beyond the limits of their hardware. As users continuously demand instruments with improved performance, the need for such algorithms will become more frequent, making extensive SL calibration campaigns increasingly critical for a broader range of space instruments. In Metop-3MI, we encountered multiple challenges simultaneously, including the presence of hundreds of ghosts and scattering patterns, variations in SL across a wide field of view, a spectral range that spans from the VNIR to the SWIR, and polarization dependencies. Despite these challenges, we achieved a new state of the art with the correction algorithm implemented in Metop-3MI. This situation, where testing methods were pushed to their utmost limits, will serve as an ideal case study for the development of future high performance instruments.

Appendices

SPST measurement setup

The collimated beam is formed by an off-axis parabola (200mm focal length, $40\times40\text{mm}^2$ aperture). Light is injected at the focal plane with an optical fiber (600µm core) at the tip of a black specular pyramid. The assembly is placed in a *MAP-PU1* coated box and the beam exits through a baffle. An *Acktar*-coated mask ($38\times38\text{mm}^2$) above the parabola limits the beam aperture. A white light source (*EQ77*) is used for VNIR channels. For SWIR channels we use: 1370 nm *Akela* laser diode, 1655 nm fiber-coupled *civil laser*, 2128 nm *CNI* laser. The collimator is placed on a translation stage and a goniometer, at about 300 mm from the instrument.

SLEP prediction

The SLEP is computed by ray tracing, considering ghosts reflections up to second order, at all wavelengths of the instrument. The instrument is illuminated by a collimated beam: a dummy surface is placed in front of the instrument and the coordinates of the rays actually generating SL reaching the detector are recorded. These coordinates constitute the SLEP footprint, which is computed for various field angles. For the experimental campaign, the spatial scan is set so that it overlaps the SLEP footprint.

Scattering model

SPST measurements performed with the SLEP encompass all ghosts, but miss a scattering contribution. The missing part is delimited outside of a rectangular zone. Using a select number of SPST measurements performed with a full spatial scan, the scattering contribution is fitted using a Harvey model $h(i,j)$ expressed by Eq. (1). The fit parameters are b, s and L. The parameters $u = i/N$ and $v = j/N$ are the pixel coordinates (i,j) normalized to the number of pixels per line or column, N. Parameters $u_0 = i_0/N$ and $v_0 = j_0/N$ are the normalized coordinates of the nominal pixel. The parameters b, s, and L are initially adjusted based on a comparison between the SLEP and full scan measurements to effectively complement the missing data in the SLEP measurement. The model is then added to the SPST maps measured with the SLEP, outside from the rectangular area.

$$h(i,j) = b \cdot \left[1 + \frac{|u-u_0|^2 + |v-v_0|^2}{L^2}\right]^{s/2} \tag{1}$$

Ghost polarization modeling

Polarization adaptation is performed by image processing on individual scan positions. First, the isolated ghost from scan position number three is integrated, and the result is plotted as a function of the azimuth angle, effectively reproducing the Malus law which is then fitted by a cosine square: $a \cdot \cos^2(\phi + d\phi)$. This provides the amplitude a and offset of the ghost's dependance with the azimuth b, and $d\phi$ is the phase which depends on the polarization orientation. When reconstructing SPST maps, we recombine the various spatial scans, modulating the ghost by the Malus fit with the phase $d\phi$ adapted to the desired polarization orientation.

SPST field-of-view interpolation

The SPST maps are measured over a calibration grid, and needs to be interpolated to a denser grid used for the correction algorithm. The interpolation goes as follows. We write $SPST_{i,j}(x,y)$ the SPST map associated to field (i,j), such that the nominal pixel is $(x,y)=(i,j)$. To deduce the SPST at any field (i_*,j_*), we apply a transformation[25] on the SPST map from the closest calibrated field (i_c,j_c): a scaling by a factor $s = r_*/r_c$ and a rotation by an angle α, where r_* and r_c are the radial distance of the nominal pixels compared to the center of the maps, and α is the azimuth difference. This displaces the various SL features and bring the nominal pixel from position (i_c,j_c) to (i_*,j_*). This can create missing signals on the edges, which are filled by applying a similar transformation to the next neighboring calibrated fields. Up to 4 neighbors are used to completely fill the missing pixels. Near nominal smoothing is performed, where we average the signal within 5 pixels from the nominal. The interpolation method was previously developed and validated using ray-traced SPST maps. The required calibration grid was also adapted to ensure that the residual error on the interpolated maps was sufficiently small to fulfill the SL correction users' requirements. Full development details on the interpolation are described in Clermont et al.[25] (2022).

Extended scene measurement

The integrating sphere (diameter 203.2 mm, 52×52mm exit aperture) is fed with a white light source (*EQ400*). Positioned approximately 300 mm above the instrument, its rotation enables the capture of extended scenes at various positions within the field of view. With an extended scene, the nominal signal is spread over m pixels

without saturation, and the SL is increased by a factor m compared to an SPST. Hence, the necessary dynamic to measure simultaneously the nominal and SL is decreased, allowing for a single shot acquisition.

Extended scene SL

When illuminated by an extended scene, the instrument measures an image $I_{mes}(x,y) = I_{nom}(x,y) + I_{SL}(x,y)$, where I_{nom} and I_{SL} are the nominal and SL contributions, respectively, and x and y are the coordinates on the detector. The SL is obtained with Eq. (2), where $SPST_{i,j}$ is the SPST map associated to field (i,j). This equation enables to estimate the SL associated to any input scene, for example here the reference extended scene.

$$I_{SL}(x,y) = \sum_{i,j} SPST_{i,j}(x,y) \cdot I_{nom}(i,j) \tag{2}$$

Extended scene SL correction

For an image I_{mes}, a first estimate of the SL is obtained with Eqs. (3). The correction algorithm then finds a first estimation of the SL-free image, I_{corr}, with Eq. (4). A second estimate is obtained by performing a second iteration, replacing I_{mes} by I_{corr} in (3).

$$I_{SLest}(x,y) = \sum_{i,j} SPST_{i,j}(x,y) \cdot I_{mes}(i,j) \tag{3}$$

$$I_{corr} = I_{mes} - I_{SLest} \tag{4}$$

SL correction error budget

The SL correction error budget starts with the initial SL level associated with the reference extended scene, as estimated in section "Reference extended scene estimated SL". After applying the SL correction algorithm, the image exhibits residual SL originating from various error contributors. The SL error from each contributor is evaluated individually, allowing us to identify the most significant ones. As shown on Fig. 8a, contributors include for example errors from dark correction, noise on SPST maps (SNR), interpolation errors, and others. At the 1 sigma percentile, we denote the error for contributor m as δ_m. The total residual SL, labelled Δ, is the statistical combination of the errors from the different contributors. This is obtained by performing a root-squared sum[49] of each δ_m, as shown in Eq. (5). The SL correction factor is the ratio of the initial SL to the residual SL error Δ.

$$\Delta = \sqrt{\sum \delta_m^2} \tag{5}$$

Figure 8a details the value of δ_m for the different contributors in the 410 nm channels. The values are derived by first assessing the error on individual SPST maps caused by a specific contributor. Since the extended scene SL is obtained by a linear combination of the SPST maps, the error on the extended scene results from combining the errors from the different SPST maps as well. For example, detector noise (SNR) introduces a random error on each SPST map. Its contribution to an individual map, ϵ, is evaluated by estimating the statistical deviation of the signal in areas of uniform signal. When computing the extended scene, the impact of the noise is a sum of random variables, thus it is obtained as a root squared sum of the error from the different maps. Since half of the scene is modulated by the bright radiance L_{max}, and half is modulated by the dark radiance L_{ref}, the error is expressed by Eq. (6), where each sum runs over half of the field of view.

$$\delta = \sqrt{\sum L_{max} \cdot \epsilon^2 + \sum L_{ref} \cdot \epsilon^2} \tag{6}$$

In addition to SNR, this principle is used to estimate the contribution from levels recombination, near-nominal smoothing, and normalization errors. However, the error from dark correction is identical for each SPST map, as the same dark map is removed for all SPST. Therefore, it contributes to an error on the extended scene obtained through a simple algebraic sum rather than a root-squared sum, as expressed in Eq. (7).

$$\delta = \sum L_{max} \cdot \epsilon + \sum L_{ref} \cdot \epsilon \tag{7}$$

For channels at polarization orientations of 60° or 0°, level L3 is obtained by applying a transformation to the measurements from the channel at − 60°. Therefore, they present an additional error contribution due to the polarization transformation. In this case, we can't evaluate the error on a single map and use Eq. (6) to assess the impact on the extended scene, as the error is not purely random. Similarly, Eq. (7) cannot be used because the error has a complex dependence on the field angle. Therefore, an alternative approach is used; For validating the polarization transformation, SPST were measured for 108 field angles for all polarization orientations (Φ in steps of 30° and θ in steps of about 5°). A simplified extended scene is obtained by summing all these maps. Comparing this scene when considering the measured maps at 0° or 60° with the maps transformed based on the − 60° measurement gives an estimate of the extended scene polarization error. Depending on the channel, the relative polarization error is between 1.1% and 3.6% (as mentioned in Section "SPST polarization dependence"). Multiplying this relative error by the initial SL on the extended scene gives the absolute error listed in Fig. 8a, giving between 0.22% and 0.79% depending on the channel. In addition, we have a negligible error coming from a residual polarization of the input beam.

Regarding SPST maps interpolation, we found that it introduces ghost displacement errors up to approximately 3 pixels (see section "SPST field-of-view interpolation"). This result aligns with previous analyses conducted using ray tracing simulations[25]. Consequently, the error contribution from interpolation restricts the correction factor to the predicted × 119, as previously demonstrated by ray tracing simulations[25]. Finally, the algorithm employs 2 iterations and a 128 pixels binning, a choice which was made during the theoretical algorithm development[25]. The impact of algorithm convergence and binning is evaluated by comparing the extended scene estimated with 2 iterations and considering binning, with the result obtained at convergence and with no binning.

Data availability

The datasets generated during and/or analyzed during the current study are not publicly available because they are proprietary to the mission but are available from the corresponding author on reasonable request.

Received: 25 May 2024; Accepted: 29 July 2024
Published online: 22 August 2024

References

1. Thompson, K. P. & Rolland, J. P. Freeform optical surfaces: A revolution in imaging optical design. *Opt. Photon. News* **23**(6), 30–35. https://doi.org/10.1364/OPN.23.6.000030 (2012).
2. Norman, A. *et al.* Advanced manufacturing for space applications. *CEAS Space J* **15**, 1–6. https://doi.org/10.1007/s12567-022-00477-6 (2023).
3. Rochus, P. *et al.* New applications of rapid prototyping and rapid manufacturing (RP/RM) technologies for space instrumentation. *Acta Astronaut.* **61**(1–6), 352–359. https://doi.org/10.1016/j.actaastro.2007.01.004 (2007).
4. Yung, K.-L., Tang, Y.-M., Ip, W.-H. & Kuo, W.-T. A systematic review of product design for space instrument innovation, reliability, and manufacturing. *Machines* **9**, 244. https://doi.org/10.3390/machines9100244 (2021).
5. Fest, E. *Stray Light Analysis and control* (SPIE Press, Bellingham, 2013). https://doi.org/10.1117/3.1000980.
6. Breault, R. P. *Control of Stray Light*, Chap 38 in Handbook of Optics Vol. 1 (eds: Bass, M., Van Stryland, E. W., Williams, D. R., Wolfe, W. L.) 38.1–38.35 (McGraw-Hill, USA, 1995)
7. Kirschner, V. Stray light analysis and minimization, unpublished tutorial from Space Optics Instrument design & technology (SOID) (Poltu Quatu, 2017)
8. Park, J.-O., Jang, W.-K., Kim, S.-H., Jang, H.-S. & Lee, S.-H. Stray light analysis of high resolution camera for a low-earth-orbit satellite. *J. Opt. Soc. Korea* **15**, 52–55 (2011).
9. Wang, G., Xing, F., Wei, M. & You, Z. Rapid optimization method of the strong stray light elimination for extremely weak light signal detection. *Opt. Express* **25**, 26175–26185 (2017).
10. Romoli, M., Weiser, H., Gardner, L. & Kohl, J. Stray-light suppression in a reflecting white-light coronagraph. *Appl. Opt.* **32**, 3559–3569. https://doi.org/10.1364/AO.32.003559 (1993).
11. Zhang, G. *et al.* Stray-light suppression of the internally occulted reflecting solar corona imager. *Front. Phys.* **10**, 890197. https://doi.org/10.3389/fphy.2022.890197 (2022).
12. Galano, D., et al. Development of ASPIICS: A coronagraph based on Proba-3 formation flying mission. In *Proceedings of SPIE 10698, Space Telescopes and Instrumentation 2018: Optical, Infrared, and Millimeter Wave*, 106982Y (2018) https://doi.org/10.1117/12.2312493
13. Renotte, E., et al., Recent achievements on ASPIICS, an externally occulted coronagraph for PROBA-3. In *Proceedings of SPIE 9904, Space Telescopes and Instrumentation 2016: Optical, Infrared, and Millimeter Wave*, 99043D (2016) https://doi.org/10.1117/12.2232695
14. Defise, J. M. Design and tests for the heliospheric imager of the STEREO mission. In *Proceedings of SPIE 4853, Innovative Telescopes and Instrumentation for Solar Astrophysics* (2003) https://doi.org/10.1117/12.460361
15. Eyles, C. J. *et al.* The heliospheric imagers onboard the STEREO mission. *Sol. Phys.* **254**, 387–445. https://doi.org/10.1007/s11207-008-9299-0 (2009).
16. DeForest, C. E. & Howard, T. A. Feasibility of heliospheric imaging from near Earth. *Astrophys. J.* https://doi.org/10.1088/0004-637X/804/2/126 (2015).
17. Thernisien, A., et al. Stray light analysis and testing of the SoloHI (solar orbiter heliospheric imager) and WISPR (wide field imager for solar probe) heliospheric imagers. In *Proceedings of SPIE 10698, Space Telescopes and Instrumentation 2018: Optical, Infrared, and Millimeter Wave*, 106980E (2018) https://doi.org/10.1117/12.2313645
18. Gauvin, M. A. & Freniere, E. R. Reducing stray light in Opto-Mechanical Systems. In *2nd International Conference on Optical Design and Fabrication*, 277–280 (2000).
19. Grabarnik, S. Optical design method for minimization of ghost stray light intensity. *Appl. Opt.* **54**, 3083–3089 (2015).
20. Buchheister, J. & Weth, C. Lens design with suppressed first order reflections. *Proc. SPIE* **7652**, 76522V (2010).
21. Rogers, J. D. *et al.* Removal of ghost images by using tilted element optical systems with polynomial surfaces for aberration compensation. *Opt. Lett.* **31**, 504–506 (2006).
22. Clermont, L. & Aballea, L. Stray light control and analysis for an off-axis three-mirror anastigmat telescope. *Opt. Eng.* **60**(5), 055106. https://doi.org/10.1117/1.OE.60.5.055106 (2021).
23. Plesseria, J. Y., et al. Utilisation of acktar black coatings in space applications. In *International Symposium on Materials in the Space Environment* (2018).
24. Freniere, E. R.& Skelton, D. L. Use of specular black coatings in well-baffled optical systems. *Proc. SPIE* 0675 (1987).
25. Clermont, L., Michel, C. & Stockman, Y. Stray light correction algorithm for high performance optical instruments: The case of metop-3MI. *Remote Sens.* **14**, 1354. https://doi.org/10.3390/rs14061354 (2022).
26. Clermont, L. & Michel, C. Out-of-field stray light correction in optical instruments: the case of Metop-3MI. *J. Appl. Remote Sensing* **18**(1), 016508. https://doi.org/10.1117/1.JRS.18.016508 (2024).
27. Manolis, I., Bézy, J.-L., Meynart, R., Porciani, M., Loiselet, M., Mason, G., Labate, D., Bruno, U., & De Vidi, R. The 3MI instrument on the Metop second generation. In *Proceedings of SPIE 10563, International Conference on Space Optics—ICSO* 2014, 1056324 (2017) https://doi.org/10.1117/12.2304182
28. Fougnie, B., Marbach, T., Lacan, A., Schluessel, P., Lang, R., Poli, G., Munro, R. The 3MI mission on-board EPS-SG: A multi-spectral multi-polarization multi-directional imager for operational characterization of aerosol and cloud. In *Proceedings of SPIE 10764, Earth Observing Systems* XXIII, 107640L (2018); https://doi.org/10.1117/12.2320254
29. Fougnie, B. *et al.* The multi-viewing multi-channel multi-polarisation imager—Overview of the 3MI polarimetric mission for aerosol and cloud characterization. *J. Quant. Spectrosc. Radiat. Trans.* **219**, 23–32. https://doi.org/10.1016/j.jqsrt.2018.07.008 (2018).
30. Clermont, L. *et al.* Stray light entrance pupil: An efficient tool for stray light characterization. *Opt. Eng.* **59**(2), 025102 (2020).

31. Clermont, L. *et al.* The stray-light entrance pupil concept and how it can be used to facilitate stray-light characterization. *Proc. SPIE* **11103**, 111030H (2019).
32. Stover, J. C. *Optical Scattering: Measurement and Analysis* (SPIE Press, Bellingham, 2012). https://doi.org/10.1117/3.975276.
33. Rieger, L. A., Zawada, D. J., Bourassa, A. E. & Degenstein, D. A. A Multiwavelength retrieval approach for improved OSIRIS aerosol extinction retrievals. *J. Geophys. Res. Atmosph.* **124**(13), 7286–7307. https://doi.org/10.1029/2018JD029897 (2019).
34. Michel, C., Clermont, L., Daddi, N., La China, F., Marcotte, S., Mazy, E., Porciani, M., Schmutz, F., & Stockman, Y. Multi-directional, multi-polarization, multi-spectral imager (3MI) engineering model (EM) on-ground calibration. In *Proceedings of SPIE 12188, Advances in Optical and Mechanical Technologies for Telescopes and Instrumentation* V, 121881I (2022) https://doi.org/10.1117/12.2628346
35. Laherrere, J.-M., Poutier, L., Bret-Dibat, T., Hagolle, O., Baque, C., Moyer, P., & Verges, E. POLDER on-ground stray light analysis, calibration, and correction. In *Proceedings of SPIE 3221, Sensors, Systems, and Next-Generation Satellites*, (1997) https://doi.org/10.1117/12.298073
36. Yeo, K. L. *et al.* Point spread function of SDO/HMI and the effects of stray light correction on the apparent properties of solar surface phenomena. *Astron. Astrophys.* https://doi.org/10.1051/0004-6361/201322502 (2014).
37. Richardson, W. H. Bayesian-based iterative method of image restoration. *J. Opt. Soc. Am.* **62**, 55 (1972).
38. Lucy, L. B. An iterative technique for the rectification of observed distributions. *Astron. J.* **79**, 745 (1974).
39. Montanaro, M. *et al.* Stray light artifacts in imagery from the landsat 8 thermal infrared sensor. *Remote Sens.* **6**, 10435–10456 (2014).
40. Montanaro, M. *et al.* Toward an operational stray light correction for the landsat 8 thermal infrared sensor. *Appl. Opt.* **54**(13), 3963–3978 (2015).
41. Montanaro, M. *et al.* Performance of the proposed stray light correction algorithm for the Thermal Infrared Sensor (TIRS) onboard Landsat 8. *Proc. SPIE* **9972**, 99720F (2016).
42. Mora, A., Biermann, M., Bombrun, A., Boyadjian, J., Chassat, F., Corberand, P., Davidson, M., Doyle, D., Escolar, D., Gielesen, W., Guilpain, T., Hernandez, J., Kirschner, V., Klioner, S. A., Koeck, C., Laine, B., Lindegren, L., Serpell, E., Tatry, P., & Thoral, P. Gaia: focus, straylight and basic angle. In: *Proceedings of SPIE 9904, Space Telescopes and Instrumentation 2016: Optical, Infrared, and Millimeter Wave*, 99042D (2016) https://doi.org/10.1117/12.2230763
43. European Space Agency. Seeking Euclid's hidden stars; commissioning looks up. ESA Science & Exploration. https://www.esa.int/Science_Exploration/Space_Science/Euclid/Seeking_Euclid_s_hidden_stars_commissioning_looks_up. Accessed 05 April 2024
44. Abdon, S., Armand, D., Laurent, F., Barillot, M., D'Ottavi, A., Coppo, P., De Luca, E., Gabrieli, R., Bouvet, M., François, M., & Taccola, M. Digital correction of residual straylight in FLEX images. In *Proceedings of SPIE 11180, International Conference on Space Optics—ICSO 2018*, 111804G (2019) https://doi.org/10.1117/12.2536079
45. Montrone, L., Aballea, L., Bernaerts, D., Navarro-Reyes, D., Santandrea, S., Saillen, N., Sarna, K., Holbrouck, P., Moelans, W., Kendall, D., Mollet, D., De Nutte, R., Demidov, S., Saari, H., Ward, J., Kassel, R., Fussen, D., Dekemper, E., Neefs, E., & Vanhamel, J. Technological innovation for the ALTIUS atmospheric limb sounding mission. In *Proceedings of SPIE 11151, Sensors, Systems, and Next-Generation Satellites* XXIII, 111510S (2019) https://doi.org/10.1117/12.2533151
46. Born, M. & Wolf, E. *Principles of Optics: Electromagnetic Theory of Propagation, Interference and Diffraction of Light* (Elsevier, New York, 2013).
47. Goodman, J. *Introduction to Fourier Optics* 3rd edn. (Roberts and Company Publishers, Greenwood Village, 2004).
48. Collett, E. *Field Guide to Polarization* (SPIE Press, Bellingham, 2005). https://doi.org/10.1117/3.62614148.
49. Lightsey, P. A., & Arenberg, J.W. Systems Engineering for Astronomical Telescopes. SPIE Press (2018)

Acknowledgements

This study was funded by ESA/Leonardo under contract 4500511744/MetOp-SG/CSL. The authors are grateful for the meaningful discussions on these results with *Leonardo*, *EUMETSAT* and *ESA*.

Author contributions

L.C. established the concepts, defined experimental requirements, processed results, and developed and evaluated the correction algorithm. C.M. handled system engineering and automated the test campaign. Y.Z. monitored the daily operations of the test campaign. Q.C. performed the levels recombination for the SWIR SPST maps. The paper was written by L.C. and reviewed by L.C. and C.M.

Competing interests

The authors declare no competing interests.

Additional information

Correspondence and requests for materials should be addressed to L.C.

Reprints and permissions information is available at www.nature.com/reprints.

Publisher's note Springer Nature remains neutral with regard to jurisdictional claims in published maps and institutional affiliations.